GEOPHYSICS, VOL. 74, NO. 1 (JANUARY-FEBRUARY 2009); P. D37–D48, 15 FIGS., 2 TABLES.
10.1190/1.3036009

Converted-wave splitting estimation and compensation

James L. Simmons Jr.[1]

ABSTRACT

Converted-wave (C-wave) splitting estimation and compensation (SEAC) estimates and removes the effects of shear-wave splitting from C-wave data. A locally 1D earth is assumed where a priori rotation of the field data to radial-transverse coordinates is valid. Subsurface fractures (horizontal transverse isotropy [HTI] layers are assumed) polarize C-wave reflection energy onto the transverse component, and introduce azimuth-dependent traveltime variations to the radial component. SEAC estimates the fast principal direction of the fractures, and the amount of traveltime splitting, from input radial and transverse azimuth-sectored stacks. SEAC also produces a splitting-compensated radial component, and a data misfit transverse component. Local fracture variations not accounted for in the coarse-interval inversion may be interpreted in the data misfit. Synthetic data generated by anisotropic reflectivity modeling for a model containing two HTI layers having different principal directions was used to illustrate SEAC. The field data example used was from a large 3-C, 3D Vectorseis survey from onshore China. Preprocessed C-wave data (radial and transverse components) were prestack time migrated into offset planes within 10-degree azimuth sectors. These data were then corrected for residual moveout (azimuth-independent correction), and stacked over offset to produce azimuth-sectored stack gathers that were input to SEAC. SEAC estimated the azimuth of the fast principal direction ϕ_{fast} and the amount of traveltime splitting Δt_{split} that describe the overburden anisotropy. Spatially variable parameter estimates for the entire 3D data set, ($\phi_{fast} = 90° \pm 20°$ and $\Delta t_{split} = 28 \pm 20$ ms), produce significantly reduced energy on the transverse component at all record times after inversion. Azimuth-dependent traveltime variations on the input radial data were also significantly reduced at all record times, resulting in a postinversion radial full-azimuth stack having improved reflection continuity and temporal bandwidth. The data misfit (transverse component after inversion) potentially revealed local variations in shear-wave splitting not accounted for by the overburden layer-stripping correction.

INTRODUCTION

Converted waves (C-waves) are especially sensitive to subsurface fractures in that both traveltime and polarization are generally affected. I assume that the form of anisotropy under consideration is transverse isotropy with a horizontal symmetry axis (HTI), representative of vertical fractures in an otherwise isotropic background. Vertical fractures cause the propagating shear waves to be polarized into a fast shear wave (S_1) parallel to the fracture strike, and a slow shear wave (S_2) perpendicular to the fracture strike. Upon propagation through an anisotropic medium (as opposed to simply reflecting from the top of an HTI layer), a shear wave will be split into a fast component and a slow component and will accumulate a delay time between the orthogonally polarized components (Keith and Crampin, 1977).

The fast direction ϕ_{fast} represents the polarization direction of the fast shear wave, and the delay time Δt_{split} represents the time difference between the fast and slow arrivals. When Δt_{split} is small relative to the dominant seismic wavelength, the fast and slow waves interfere, and the resulting seismic trace is complicated and of poor temporal resolution. For a medium containing several HTI layers where ϕ_{fast} varies with depth, each propagating shear mode will, upon encountering such a different layer, split into two modes, each aligned according to the anisotropy in the new layer. The seismic trace is particularly complex, and top-down layer stripping is required to expose the true subsurface reflection response.

Many inverse problems have been developed, in both the classical seismology (earthquake) and exploration seismology literature, to attempt to estimate ϕ_{fast} and Δt_{split} from multicomponent seismic data. Earthquake data analysis generally involves single receiver-station techniques. Single station earthquake splitting analysis is complicated by the fact that the incoming waves' polarization (azimuthal direction) must generally be estimated. The process then consists of a rotation to radial and transverse components, followed

Manuscript received by the Editor 25 January 2008; revised manuscript received 25 June 2008; published online 30 December 2008.
[1]GX Technology, a subsidiary of ION Geophysical Corporation, Denver, Colorado, U.S.A. E-mail: jim.simmons@iongeo.com.

by a rotation to fast, slow components based on an estimate of ϕ_{fast}, estimation of Δt_{split}, a time shift of $-\Delta t_{split}$ to the slow component, and finally an inverse rotation.

An excellent and concise review of these splitting-estimation approaches applied to earthquake data is given by Long (2006). Vidale (1986) demonstrates that the inverse-splitting operator can be found from the time-domain covariance matrix of the horizontal particle motion. Silver and Chan (1991) grid search for the best-fitting (ϕ_{fast}, Δt_{split}) that produces the most nearly singular covariance matrix between the splitting-corrected horizontal components. A similar method, based on maximizing the crosscorrelation between corrected components, is used by Fukao (1984), Bowman and Ando (1987), and Levin et al. (1999).

A multichannel technique applied to earthquake data is presented by Chevrot (2000). Splitting-model parameters are estimated from the relative amplitudes of the radial and transverse components as a function of the polarization angle of the incoming wave.

Applications of shear-wave splitting in the exploration context began with the pioneering work of Alford (1986). Input data are 2C $\times$ 2C (two orthogonal shear-wave sources, and two orthogonal horizontal receivers), and the inverse problem involves estimating ϕ_{fast} such that the fast and slow shear waves appear on separate data components. Crosscorrelation of the fast and slow data then give estimates of Δt_{split}. Although the Alford rotation theory is only strictly valid for a single anisotropic layer (Thomsen, 1988), it is often applied in a layer-stripping fashion (Winterstein and Meadows, 1991a, b; Thomsen et al., 1995a, 1995b). A method that attempts to estimate the splitting parameters across a depth interval without the need for top-down layer stripping is presented by Lefeuvre et al. (1992). Extensions of the 2C $\times$ 2C Alford rotation to single-source vertical seismic profiling (VSP) and C-wave data are given by Thomsen et al. (1999).

Wide-azimuth 3D C-wave data can be analyzed to expose, and correct for, the effects of shear-wave splitting. The incoming polarization of the reflected wave is known when radial and transverse data are segmented by source-receiver azimuth. C-wave splitting signatures are most easily identified after azimuth-independent NMO correction, azimuth sectoring, and stacking over offset. The transverse component will be nonzero (assuming a locally 1D earth), and reflections reverse polarity at 90-degree azimuth intervals. A given reflection on the radial component will show a sinusoidal-like traveltime variation as a function of azimuth if Δt_{split} is large enough. Note that the transverse component is sensitive for $\Delta t_{split} > 0$, and a simple reflection from an isotropic/HTI interface will polarize energy onto the transverse component, even though the wave has not propagated into the HTI layer (i.e., no traveltime splitting).

A common way to detect ϕ_{fast} from C-wave data that are well sampled in azimuth is to search for the azimuthal directions at which the transverse component has an amplitude null (Li, 1998). These amplitude nulls give the principal directions parallel ϕ_{fast} and perpendicular ϕ_{slow} to the fracture strike. For data with poorer azimuthal coverage, Bale et al. (2005) develop a least-mean-squared error approach, similar to that of Chevrot (2000), to estimate ϕ_{fast} from the transverse component. If multiple HTI layers are present, these approaches require layer stripping to accurately estimate ϕ_{fast} for the deeper layers.

The 2C $\times$ 2C rotation analysis and layer-stripping technique of Alford is extended to 3D C-wave data by Gaiser (1999). Orthogonal source and receiver pairs are simulated from the 2C radial and transverse azimuth-sectored stacks to construct the 2C $\times$ 2C Alford data matrix. Processing then follows the approach of Alford (1986). Poststack layer-stripping procedures are applied to synthetic prestack C-wave data by Gumble and Gaiser (2006) to quantify the errors in estimating the seismic splitting parameters from poststack data.

Splitting estimation and compensation (SEAC) is applied to C-wave data from a high quality, wide-azimuth 3-C, 3D Vectorseis survey from the Sichuan Basin, onshore China. The inverse problem follows the general approach of Silver and Chan (1991), whereby optimal ϕ_{fast} and Δt_{split} estimates are obtained from prestack time-migrated (PSTM) radial and transverse azimuth-sectored stacks. These model parameter estimates best account for the radial component azimuthally dependent traveltimes, and transverse component energy over the analysis time window.

Main contributions are emphasis on an improved radial component data set because the splitting effects are removed, and the data misfit, which is the energy remaining on the transverse component after inversion. The data misfit has the potential to expose local splitting anomalies not predicted in the rather coarse, interval-style inversion.

SEAC is formulated and demonstrated on synthetic data generated by anisotropic reflectivity modeling. The earth model consists of a number of isotopic layers along with two HTI layers that have different principal directions.

Results from three inlines of the field data set illustrate the improved quality of the compensated radial full-azimuth stack after inversion for the overburden splitting. The overburden inversion reduces the transverse component energy, and provides potentially interpretable data that highlight anomalies relative to the estimated-splitting model. Maps of the model parameter estimates for the entire 3D data set, $\phi_{fast}(x,y)$ and $\Delta t_{split}(x,y)$, show the spatial variability in the apparent overburden shear-wave splitting.

MOTIVATION: C-WAVE SPLITTING IN FIELD DATA

A wide-azimuth, wide-offset 3-C, 3D Vectorseis survey from onshore China is the field data set used to demonstrate SEAC. Prior 3D P-wave surveys did not provide sufficient information to characterize the reservoir fracturing thought to be controlling hydrocarbon production. Preliminary processing of a single swath of the 3-C, 3D data revealed azimuthally dependent traveltime variations on the radial component azimuth-sectored common conversion point (CCP) stacks, and significant energy on the transverse data, at all reflection times. Full-azimuth radial CCP and PSTM stacks, consequently, were of low temporal resolution because the apparent splitting effects were not compensated at this stage.

Radial and transverse components of the complete 3-C, 3D data set are processed with a surface-consistent amplitude preserving flow. PSTM is applied to the radial and transverse components after azimuth sectoring (10-degree nonoverlapping azimuth bins), with offset preserved in the migration. Azimuth-independent residual-moveout corrections are then applied to the PSTM gathers. Data within each azimuth sector are then stacked over offset to produce radial and transverse azimuth-sectored stack gathers for each inline-crossline bin. Each gather consists of 36 traces, corresponding to central azimuthal angles of $\theta = -170, -160, \ldots, 170, 180$ degrees, where north=0 degrees, and east=90 degrees. The output image volume is approximately 20 $\times$ 20 km.

Representative radial and transverse PSTM azimuth-sectored stack gathers are shown in Figure 1. Reflection traveltime variations

with azimuth are seen on the radial data (Figure 1a). The transverse data, meanwhile, are nonzero, and generally have polarity reversals every 90 degrees (Figure 1b). The regional stress direction in the basin is thought to be approximately due east, which corresponds to $\phi_{\text{fast}} = 90$ degrees.

Many C-wave splitting approaches assume that this regional stress direction is necessarily correct, laterally invariant, and that the radial and transverse data are implicitly sensitive to the presumed stress field. SEAC estimates the optimal ϕ_{fast} and Δt_{split} as a function of spatial position for each input pair of radial and transverse azimuth-sectored stacks.

SYNTHETIC DATA

Anisotropic reflectivity modeling

Three-component synthetic prestack data are simulated using anisotropic reflectivity modeling. The earth model consists of horizontal, homogeneous layers, where any or all layers may be generally anisotropic. Three-component geophones are equally spaced in x and y over a square grid from $-x_{\max} \le x \le x_{\max}$, and $-y_{\max} \le y \le y_{\max}$, at a constant receiver depth (in this case, $z = 0$). An explosive source (force sources in x, y, z can also be used) is located at the center of the grid at $x = 0, y = 0, z = 5$ m.

Three-dimensional 3-C prestack data cubes for the (x, y, z) receiver components are produced. Plane waves are propagated through the layered medium for all wavenumbers (positive and negative) k_x and k_y, and temporal frequencies ω. Negative wavenumbers are needed to properly simulate source-receiver azimuth effects, properly model source directivity in the case of horizontal-force sources, and to generate the seismic response in generally anisotropic media (Fryer and Frazier, 1984, 1987). The recursion relations of Kennett (1983) propagate the the plane waves through the layered medium, and produce the complete plane-wave response. Because the plane-wave reflection response of the medium is equally sampled in (ω, k_x, k_y), a 3D inverse Fourier Transform produces the 3-C prestack data cubes in the time-space domain, (t, x, y).

All wave modes are generated by the reflectivity modeling; primary reflections, C-waves, head waves, all interbed multiples, as well as surface multiples and surface waves depending on whether free surface effects are included. Free surface effects and attenuation are not included in the simulation shown here.

The earth model consists of two HTI layers having different principal directions, and a number of isotropic layers (Tables 1 and 2). An explosive source simulates 3-C data recorded over a grid from -7500 to 7500 m in x and y, with a 50-m trace spacing in each direction. The source is located at the center of the grid at coordinates ($x = 0, y = 0$). Horizontal receiver components are oriented in the $+x$ and $+y$ directions (east and north).

Horizontal receiver components R_x and R_y for two receiver lines are shown in Figure 2a and b. Offset refers to the actual source-receiver offset, and is noted as signed offset in Figure 2a. The expected polarity reversal from positive to negative offsets is seen on R_x in Figure 2a. The fact that $R_y \neq 0$ indicates the presence of splitting, with the principal directions of the HTI layers rotated relative to the (x, y) acquisition-coordinate axes. Splitting polarizes the C-waves onto R_y. P-wave arrivals (direct wave, refractions, reflections) are contained on R_x.

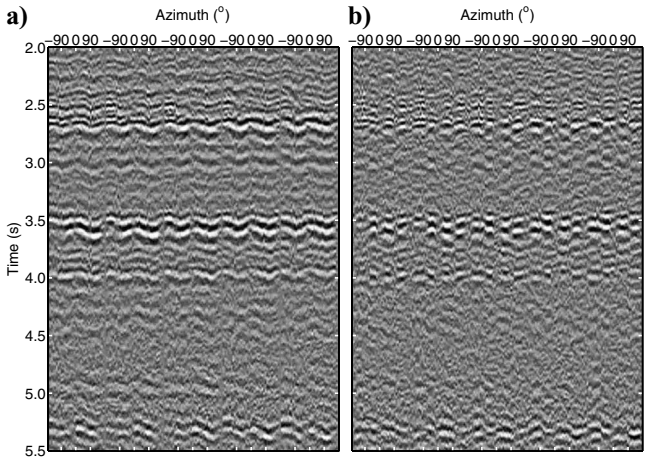

Figure 1. Expanded view of five azimuth-sectored stack gathers showing the apparent C-wave splitting signatures in the field data. Each gather consists of 36 traces. The azimuth sector is indicated at the top, north = 0°, east = 90°, west = −90°. (a) Radial component. (b) Transverse component.

Table 1. Model parameters for the synthetic example. Layers 3 and 6 are HTI specified in terms of C_{ij} in Table 2. V_P and V_S are the P-wave and S-wave velocities, ρ is the bulk density, Δz is the layer thickness, z is the depth, and ϕ_{fast} is the azimuth of the fast direction measured in degrees clockwise from north. Vertical two-way traveltimes for the P-wave and C-wave reflections to the bottom of each layer are denoted as (t_{PP} and t_{PS}). The interval two-way vertical traveltimes ($\Delta t_{PP}, \Delta t_{PS}$) refer to the fast direction for the HTI layers.

Layer	V_P (m/s)	V_S (m/s)	ρ (kg/m^3)	Δz (m)	z (m)	Δt_{PP} (s)	Δt_{PS} (s)	t_{PP} (s)	$t_{PS}(s)$	ϕ_{fast}
1	2000	1000	2.00	200	200	0.200	0.300	0.200	0.300	—
2	3410	2010	2.48	1500	1700	0.880	1.186	1.080	1.486	—
3-HTI	4337	2224	2.60	150	1850	0.069	0.102	1.149	1.588	60
4	3410	2010	2.48	200	2050	0.117	0.158	1.266	1.746	—
5	3000	1500	2.10	200	2250	0.133	0.200	1.400	1.946	—
6-HTI	4337	2224	2.60	150	2400	0.069	0.102	1.469	2.048	25
7	3410	2010	2.48	100	2500	0.059	0.080	1.527	2.127	—
8	3000	1500	2.10	100	2600	0.067	0.100	1.594	2.227	—
9	3410	2010	2.48	—	—	—	—	—	—	—

When the receiver line is not along the $y = 0$ axis (Figure 2b), R_x no longer shows the expected polarity reversal across the near offset for all events because of the C-wave splitting. Events at two-way vertical traveltimes of $t \leq 1.8$ *s* are P-waves, and do show the polarity reversal. P-wave and C-wave arrivals are now contained on both receiver components.

Rotation of the data to radial-transverse coordinates, R_R and R_T, is shown in Figure 2c and d, respectively. All P-wave energy is contained on R_R, and R_T exposes the split C-waves.

Azimuth-sectored stacks

Traveltime variations as a function of offset and azimuth produced by the HTI layers are illustrated on radial and transverse component azimuth-sectored stacks (Figure 3). A gain correction of $t^{1.8}$ is applied to the prestack data volumes, followed by an approximate three-term normal-moveout correction using azimuth-independent moveout parameters, an outside trace-mute, and azimuth sectoring (10-degree sectors). A stack over offset within each azimuth sector produces azimuth-sectored stack gathers for R_R and R_T. The vertical bars at the left in Figure 3a indicate the HTI (black) and isotropic (gray) layers of the model, with the length of the bars indicating the two-way vertical traveltime thickness.

Behavior of the radial and transverse components as a function of source-receiver azimuth can now be seen clearly. The principal directions for the shallow HTI layer can be inferred from $R_T \approx 0$ for the reflections at 1.588 and 1.746 s. Meanwhile, R_R reveals the fast and slow directions ($\phi_{\text{fast}} = 60°$, $\phi_{\text{slow}} = -30°$) from the traveltime minima and maxima along these reflections, respectively.

Increased traveltime variation with azimuth can be seen for the reflections at $t_{PS} \approx 2.048$, 2.127, and 2.227 s because these events have also propagated through the deeper HTI layer.

The transverse component (Figure 3b) nicely shows the principal directions for the shallow HTI layer by the amplitude nulls. At azimuths θ between the principal directions, the amplitude of R_T increases and then decreases, reaching maximum amplitude when $\theta = \pm 45°$ relative to the principal directions. Principal directions of the deeper HTI layer cannot be inferred directly from R_T.

Additional energy apparent from 1.84 to 1.93 s, and just above the base of the deep HTI layer (near 2.0 s) are some combination of coda (interbed multiples, local C-waves, etc.).

Also note that the reflection from the top of the shallow HTI layer ($t_{PS} = 1.486$ s) is apparent on the transverse component. This reflection is polarized onto the transverse component by the HTI in the lower layer, but traveltime splitting has not yet occurred.

If the two HTI layers had the same principal directions, R_T would have well-defined amplitude nulls at the principal direction azimuths for all reflection events. Because the principal directions of the HTI layers differ, the response for events at $t_{PS} \geq 2.0$ s becomes complicated. To isolate the deeper splitting effects in Figure 3a and b, the principal direction, ϕ_{fast}, and the amount of traveltime splitting, Δt_{split}, must be estimated for the shallow HTI layer. The shallow-layer splitting effects can then be removed from the data in Figure 3 to isolate the deeper splitting on the radial and transverse azimuth-sectored stacks.

The general form of the input data to the SEAC algorithm are azimuth-sectored stack gathers as in Figure 3 for each analysis location. Data can be azimuth-sectored CCP stacks, or azimuth-sectored PSTM stacks. The inverse problem attempts to estimate the splitting-model parameters, ϕ_{fast}, and the amount of traveltime splitting, Δt_{split}, for each input gather pair, and also produces splitting-compensated radial and transverse component data sets.

Table 2. C_{ij} for HTI layers 3 and 6 in Voigt notation. The C_{ij} are rotated by the appropriate ϕ_{fast} for the reflectivity modeling.

C =	44.4152	21.7204	21.7204	0.0	0.0	0.0
	—	48.920	23.1999	0.0	0.0	0.0
	—	—	48.920	0.0	0.0	0.0
	—	—	—	12.8601	0.0	0.0
	—	—	—	—	10.5039	0.0
	—	—	—	—	—	10.5039

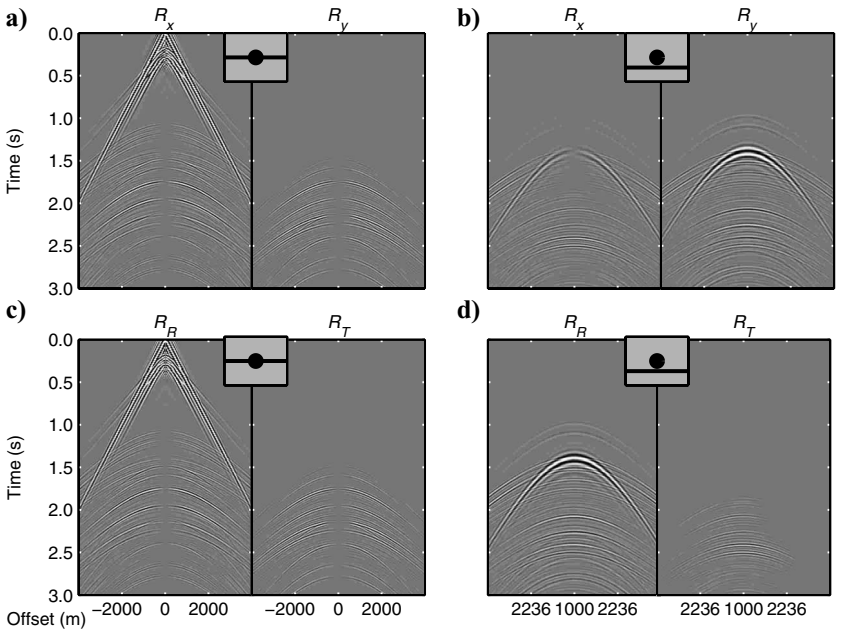

Figure 2. Synthetic data, prestack shot gathers of horizontal receiver components for the receiver lines indicated on the base map. The shot location is at $x = 0$, $y = 0$ and is indicated by the black circle. (a) Gathers R_x and R_y recorded along the $y = 0$ axis. (b) Gathers R_x and R_y where the offset in the $-y$ direction is 1000 m. (c) Data recorded along the $y = 0$ axis after rotation to radial and transverse coordinates, R_R and R_T. (d) Data recorded along the receiver line offset in the $-y$ direction after rotation to radial and transverse coordinates, R_R and R_T. Shear-wave splitting, where the principal directions of the HTI layers are rotated relative to the (x,y) coordinate axes, is indicated by $R_y \neq 0$ in (a), and $R_T \neq 0$ in (c). The matrix C is symmetric, only values in the upper triangular matrix are shown.

INVERSE PROBLEM: SEAC

SEAC from radial and transverse azimuth-sectored stacks involves forward modeling and in-

version. Each trace of the azimuth-sectored stacks is associated with a particular source-receiver azimuth θ. In the context of a locally 1D earth, all energy is contained on the radial component in the presence of isotropic or polar anisotropic media, with $R_T = 0$ for all θ.

Shear-wave splitting produced by an HTI layer rotates the incident wavefield to the fast and slow directions, parallel and perpendicular, respectively, to the fracture strike, and introduces a traveltime delay Δt_{split} to the slow shear wave. An additional rotation then projects the wavefields onto the original acquisition coordinate system. As a result, a given reflection on the the radial component shows traveltime variations as a function of θ. Meanwhile, the transverse component is nonzero, and has polarity reversals at 90-degree azimuth intervals. Amplitude nulls occur on the transverse component when θ is parallel or perpendicular to the fracture strike ϕ_{fast}.

Assume that the incident wavefield $\mathbf{u}_0$ (with radial component, $u_R(t)$, and transverse component, $u_T(t)$) is propagating in the radial direction at a particular azimuth θ. The splitting forward-modeling operator is described in the frequency domain ω as (Silver and Chan, 1991)

$$\hat{\mathbf{u}}(\omega) = \mathbf{R}^{-1}\mathbf{D}\mathbf{R}\mathbf{u}_0(\omega). \tag{1}$$

Equation 1 involves the rotation of the incident wave about an angle α, where $\alpha = \phi_{\text{fast}} - \theta$ as

$$\mathbf{R} = \begin{pmatrix} \cos\alpha & \sin\alpha \\ -\sin\alpha & \cos\alpha \end{pmatrix}, \tag{2}$$

and a time delay Δt_{split} produced by the splitting

$$\mathbf{D} = \begin{pmatrix} 1 & 0 \\ 0 & e^{-i\omega\Delta t_{\text{split}}} \end{pmatrix}. \tag{3}$$

Prior to propagation through a single HTI layer, all energy is on $u_R(t)$, with $u_T(t) = 0$. The time-domain response of $\hat{u}_R(t)$ and $\hat{u}_T(t)$ in the presence of traveltime splitting Δt_{split} from a single HTI layer (for fixed θ) for traveltimes greater than the time at which the splitting occurs is

$$\hat{u}_R(t) = u_R(t)\cos^2\alpha + u_R(t - \Delta t_{\text{split}})\sin^2\alpha, \tag{4}$$

$$\hat{u}_T(t) = u_R(t)\sin\alpha\cos\alpha - u_R(t - \Delta t_{\text{split}})\sin\alpha\cos\alpha. \tag{5}$$

The radial component $\hat{u}_R(t)$ is fast when $\cos^2\alpha = 1$ ($\alpha = 0°, 180°$), and slow when $\sin^2\alpha = 1$ ($\alpha = -90°, 90°$). Along these principal directions, $\hat{u}_T(t) = 0$. When $\theta = \pm 45°$ relative to the principal directions, $\hat{u}_T(t)$ reaches its maximum value. For small Δt_{split} (relative to the dominant wavelength), $\hat{u}_T(t)$ resembles the scaled time derivative of the seismic wavelet. These characteristics can be seen for the shallower events in Figure 3.

For multiple HTI layers in the travel path, equation 1 would include a cascade of the appropriate rotation matrices $\mathbf{R}$ and traveltime splitting matrices $\mathbf{D}$ for each layer.

A straightforward solution to the inverse problem is that of a grid search over a range of trial $(\phi_{\text{fast}}, \Delta t_{\text{split}})$ values evaluated over all θ for a specified time window of data $t_{\min} \le t \le t_{\max}$. For each trial $(\phi_{\text{fast}}, \Delta t_{\text{split}})$ pair, radial and transverse azimuth-sectored stacks are rotated by the appropriate α to produce fast and slow data sets. A static shift of $-\Delta t_{\text{split}}$ is applied to the slow data set, and the fast-slow data sets are then unrotated by the appropriate α. Mathematically, the process is simply

$$\hat{\mathbf{u}}_0(\omega) = \mathbf{R}^{-1}\mathbf{D}'\mathbf{R}\hat{\mathbf{u}}(\omega), \tag{6}$$

with

$$\mathbf{D}' = \begin{pmatrix} 1 & 0 \\ 0 & e^{i\omega\Delta t_{\text{split}}} \end{pmatrix}. \tag{7}$$

The objective function is the total energy remaining on the transverse component after applying equation 6 as

$$E_T(\phi_{\text{fast}}, \Delta t_{\text{split}}) = \int_{\theta_{\min}}^{\theta_{\max}} \int_{t_{\min}}^{t_{\max}} \hat{\mathbf{u}}_T^2(t,\theta)\,dt\,d\theta. \tag{8}$$

Optimal parameter estimates, $(\hat{\phi}_{\text{fast}}, \Delta\hat{t}_{\text{split}})$ are taken from the minimum of $E_T(\phi_{\text{fast}}, \Delta t_{\text{split}})$. Application of equation 6 using $\hat{\phi}_{\text{fast}}$ and $\Delta\hat{t}_{\text{split}}$ ideally removes the effects of splitting from the input data over the time interval of interest.

Inversion of the synthetic azimuth-sectored stacks

The inversion and layer-stripping process is illustrated on the synthetic azimuth-sectored stacks of Figure 3, as seen in Figure 4. The

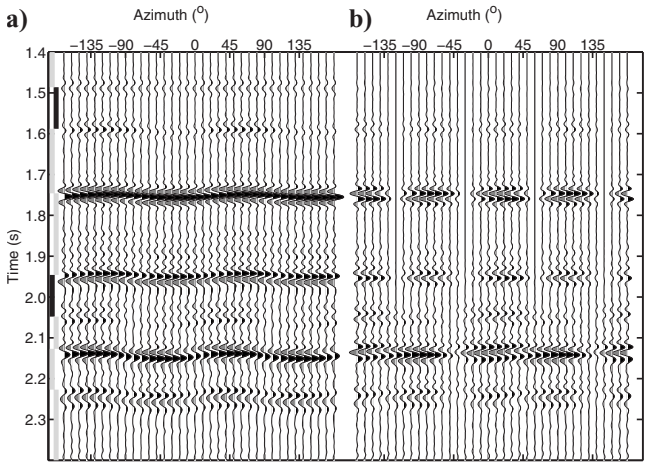

Figure 3. Azimuth-sectored stack gathers, synthetic data. (a) Radial component. (b) Transverse component. The vertical bars to the left in (a) identify the layers of the model in terms of the two-way vertical C-wave traveltime (HTI = black, isotropic = gray).

objective function $E_T(\phi_{\text{fast}}, \Delta t_{\text{split}})$ is calculated for a range of trial $\phi_{\text{fast}} = 0, \ldots, 90$, in 1-degree increments, and $\Delta t_{\text{split}} = 1, \ldots, 30$ ms, in 1-ms increments. Note that this sampling is considerably finer than that used for the field data. Parameter estimates, $\hat{\phi}_{\text{fast}}$ and $\Delta \hat{t}_{\text{split}}$, are taken from the minimum of $E_T(\phi_{\text{fast}}, \Delta t_{\text{split}})$, and are then used to apply the forward rotation, the static shift of the slow data set, and the inverse rotation expressed in equation 6 to produce the splitting-compensated radial and transverse data sets.

A shallow-interval inversion includes the data from 1.55 to 2.0 s. The splitting-compensated radial and transverse data are shown in Figure 4a and b. Reflections at $t \leq 1.946s$ now show constant traveltime as a function of azimuth on the compensated radial component of Figure 4a, except for the reflection at the top of the shallow HTI layer ($t_{\text{PS}} = 1.486$ s). This reflection is polarized onto the transverse component, although traveltime splitting has not yet occurred. As a result, the $\Delta \hat{t}_{\text{split}}$ correction suitable for the base HTI-layer reflection and deeper events, is not suitable for this event resulting in residual transverse energy (Figure 4b), and an inadequately time-aligned event in Figure 4a.

The true model parameters are $\phi_{\text{fast}} = 60$, and $\Delta t_{\text{split}} = 7.5$ ms. Energy that can be accounted for by equation 6 with estimated values of $\hat{\phi}_{\text{fast}} = 60°$ and $\Delta \hat{t}_{\text{split}} = 7$ ms, is rotated into the radial data of Figure 4a from the input transverse data (Figure 3b). As a result, energy on the transverse component after inversion is minimized over the time window $1.55 \leq t \leq 2.0$ s (Figure 4b). Energy remaining on the transverse component within the inversion time interval can be thought of as the data misfit in terms of inverse theory. Potentially, this residual transverse energy can also be thought of as a potential fracture-anomaly indicator as will be discussed regarding the field data examination.

Some residual energy remains in Figure 4b, related to the reflection amplitude variation-with-azimuth (AVA) differences between azimuth sectors. Note that although the input azimuth-sectored stack gathers are created from a finely sampled (in offset and azimuth) data cube, each azimuth bin does not necessarily have an equal offset distribution, and AVA variations for the various reflections are implicitly included in the prestack reflectivity modeling. Any coda (interbed multiples or local C-waves) will also potentially appear in Figure 4b.

Data within the shallow interval time window in Figure 4a and b are now stripped off to compose the compensated radial and transverse misfit data sets, respectively. The splitting response of the deep data is now exposed in Figure 4a and b. The deeper interval inversion operates on the data from 2.05 to 2.3 s in Figure 4a and b, and produces Figure 4c (compensated radial) and 4d (data misfit) as output. Estimated model parameters, $\hat{\phi}_{\text{fast}} = 26$, and $\Delta \hat{t}_{\text{split}} = 6$ ms, differ from the true model parameters, $\phi_{\text{fast}} = 25$ and $\Delta t_{\text{split}} = 7.5$ ms. Energy on the transverse component is minimized (Figure 4d), and the reflection traveltime alignment is improved on the compensated radial component (Figure 4c), it is not perfect.

The objective functions, $E_T(\phi_{\text{fast}}, \Delta t_{\text{split}})$, for the two-interval inversion are shown in Figure 5, with the amplitude minima indicated. It is interesting that E_T for the deep-interval inversion is somewhat broader in azimuth (Figure 5b), and more poorly defined than that of the shallow inversion (Figure 5a). The deeper interval is more affected by coda generated by the shallower data above, azimuthal NMO effects from the shallow HTI layer are imposed upon the deeper data, and the splitting response preserved in the azimuth-sectored stacks is a weighted average of the true prestack response (Gumble and Gaiser, 2006), all

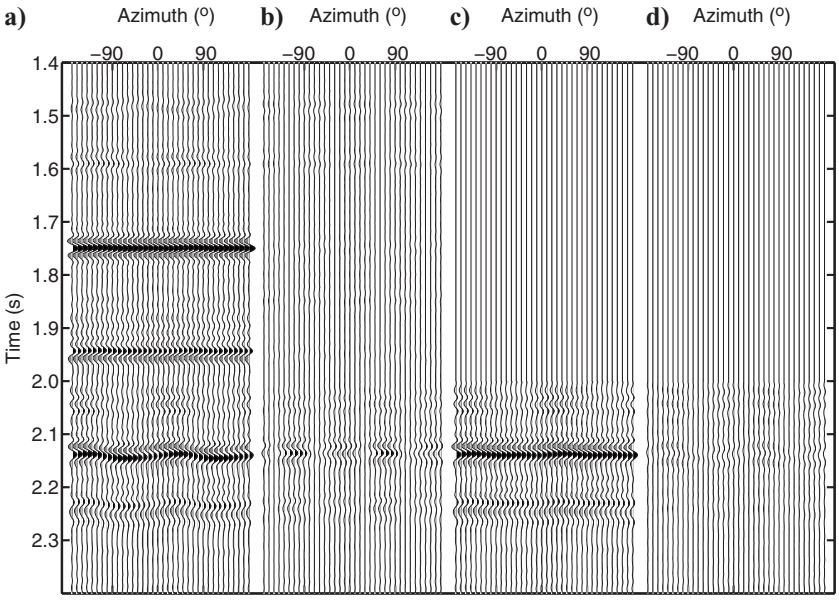

Figure 4. Synthetic inversion results, azimuth-sectored stack gathers after splitting compensation. The shallow interval is inverted over the 1.55–2.0 s time range, and the deeper interval is inverted over the 2.05–2.3 s time range. (a) Radial component after the shallow-interval inversion. (b) Transverse component after the shallow-interval inversion. (c) Radial component after the deep-interval inversion. (d) Transverse component after the deep-interval inversion.

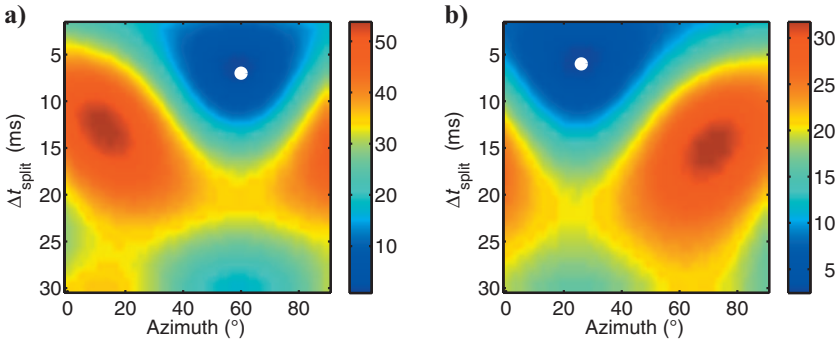

Figure 5. Objective functions for the synthetic-data inversion. The root-mean-square (rms) amplitude of the transverse component after compensation with the trial $\phi_{\text{fast}}, \Delta t_{\text{split}}$ combinations is shown. (a) Shallow-interval inversion. (b) Deep-interval inversion. The indicated amplitude minima give the optimal parameter estimates used to produce the data in Figure 4.

of which may contribute to the fact that the estimated model parameters differ from the true values.

Data sets for interpretation would be obtained from the upper 2.0 s of Figure 4a and b, and the data in Figure 4c and d. The compensated radial component is better suited for interpretation and analysis. Azimuthal traveltime variations have been corrected producing flatter azimuth-sectored stack gathers, which will result in an improved full-azimuth stack. The compensated transverse component reveals the inversion data misfit, can potentially be used as a fracture anomaly attribute, and can indicate where the input data deviate from the systematic splitting behavior seen in the radial and transverse azimuth-sectored stacks of Figures 3 and 4.

FIELD DATA EXAMPLES

Radial and transverse azimuth-sectored stack gathers along an inline near the center of the data set (line A) are shown in Figures 6a and 7a, respectively. Each subpanel is an azimuth-sectored stack gather containing 36 traces for each crossline bin. Every 10th crossline bin is shown. A main reservoir interval is from 3.6 to 4.0 s on crosslines 1325–1450. The nominal fast direction of the regional stress is due east ($\phi_{\text{fast}} \approx 90°$) based on a priori inspection of the radial and transverse azimuth-sectored stack gathers, and is also loosely supported by analysis of earthquake data (Lev et al., 2006).

The radial component gathers (Figure 6a) show traveltime variations with azimuth within each gather. Energy is apparent on the transverse component gathers (Figure 7a) throughout the section.

The time window for the overburden-splitting inversion is centered on the shallowest available mapped horizon (from the full-azimuth radial stack) near 2.5 s. A 400-ms time window below the guide horizon defines the time range for analysis. This initial inversion is designed to evaluate the extent to which overburden-splitting estimates, $\hat{\phi}_{\text{fast}}$ and $\Delta\hat{t}_{\text{split}}$, explain the splitting signatures seen on the azimuth-sectored stack gathers. Each crossline bin is inverted independently, thus, the estimated model parameters can vary spatially.

The objective function, $E_T(\phi_{\text{fast}}, \Delta t_{\text{split}})$, is evaluated for values of ϕ_{fast} from $70° \le \phi_{\text{fast}} \le 120°$, in 5-degree increments, and for values of Δt_{split} from $2.5 \le \Delta t_{\text{split}} \le 50$ ms, in 2.5-ms increments. Upper and lower parameter bounds are based on visual inspection of the input data.

Compensated radial and transverse gathers are shown in Figures 6b and 7b, respectively. Traveltime alignment of events on the radial gathers is much improved after inversion. Amplitudes have increased because transverse component energy is rotated into the compensated radial component. Energy is significantly reduced on the transverse component after inversion. Overburden-splitting corrections have accounted for most of the C-wave splitting throughout the section, from shallow to deep.

Note that for SEAC to work optimally, the input gathers should resemble the synthetic data of Figure 3. There are local areas with re-

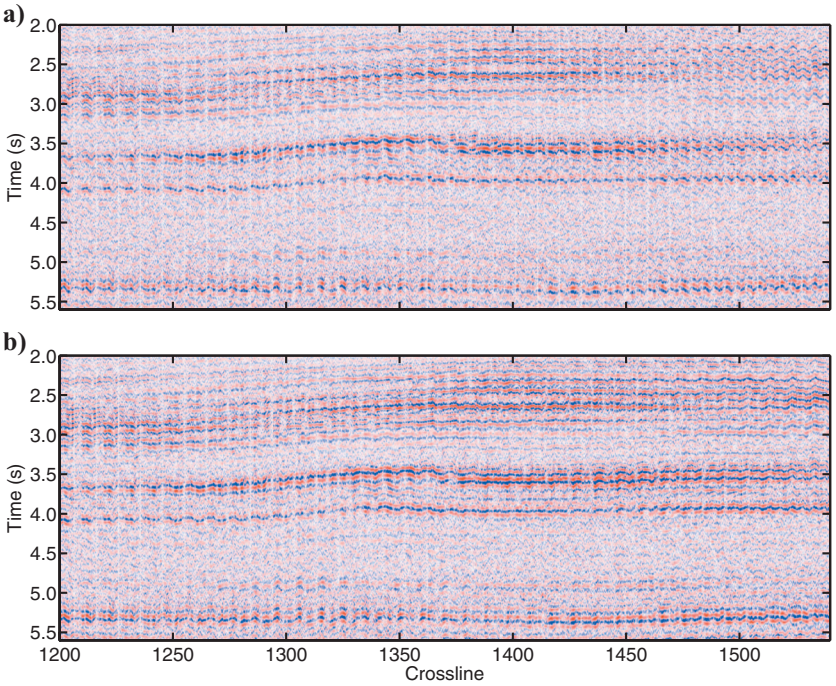

Figure 6. Field data, radial component azimuth-sectored stack gathers for line A. Each gather consists of 36 traces and every 10th crossline is shown. (a) Data input to SEAC. (b) After overburden inversion and compensation.

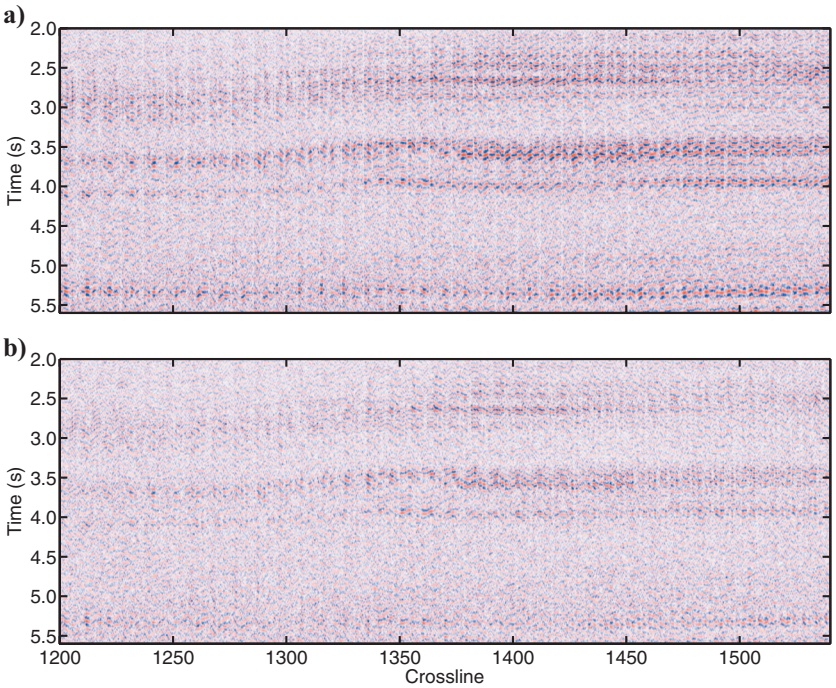

Figure 7. Field data, transverse component azimuth-sectored stack gathers for line A. Each gather consists of 36 traces and every 10th crossline is shown. The display gain is the same as that used in Figure 6. (a) Data input to SEAC. (b) After overburden inversion and compensation.

maining energy on the transverse gathers in Figure 7b, as well as radial gathers that do not show a symmetric pattern of azimuthal traveltime variations. The data misfit (Figure 7b) immediately exposes areas where the input gathers do not meet the implicit assumptions of the inversion, and/or potential areas where the splitting may be more complicated than that predicted by the model parameter estimates. Exposure and interpretation of the data misfit can be very powerful, yet is often overlooked.

Full-azimuth radial stacks are shown before and after inversion in Figure 8. Improved traveltime alignment of the radial gathers after inversion produces a stack with improved signal continuity, increased reflection amplitude, and improved spatial and temporal resolution.

A transverse component full-azimuth stack is obtained by taking the envelope of each trace prior to stacking. It is necessary to take the envelope of the individual traces because of the polarity reversals across the principal directions. Transverse component stacks before and after inversion are shown in Figure 9. This figure summarizes the amount of energy on the transverse component initially assumed to be caused by shear-wave splitting (Figure 9a), and the energy that cannot be explained (the data misfit) by the laterally variable parameter estimates, $\hat{\phi}_{\text{fast}}$ and $\Delta\hat{t}_{\text{split}}$ (Figure 9b). It is interesting that although the a priori hypothesis is that splitting potentially occurs at a number of stratal levels (overburden, main reservoir level, deeper reservoirs, etc.), a single overburden correction explains most of the energy on the transverse component, even on the basement reflection near 5.3 s. Local anomalies occur, interestingly, where there is a relatively large change in the local reflector dip (near crossline 1400).

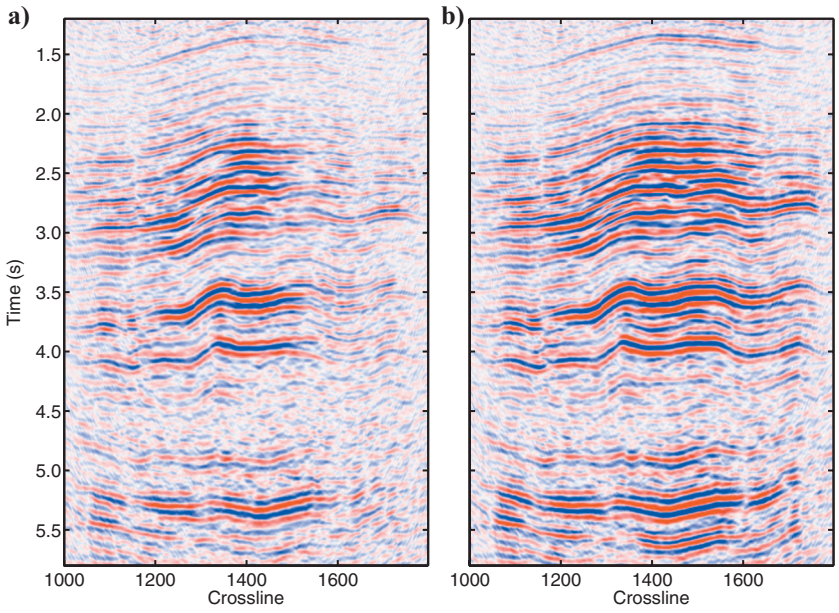

Figure 8. Radial component, full-azimuth stacks, line A. (a) Before overburden inversion and compensation. (b) After overburden inversion and compensation.

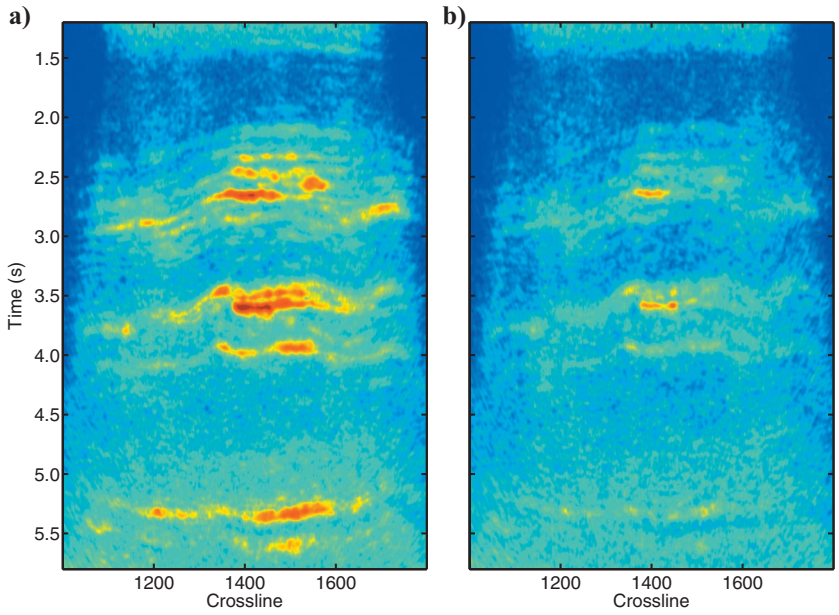

Figure 9. Transverse component, full-azimuth stacks, line A. The complex trace envelope is taken for each trace prior to stacking. (a) Before overburden inversion and compensation. (b) After overburden inversion and compensation.

Radial and transverse full-azimuth stacks before and after the overburden inversion from line B, located 6 km east of line A, are shown in Figures 10 and 11. Results from line C, located 2.5 km west of line A, are shown in Figures 12 and 13. In both cases, the full-azimuth radial stacks are much improved after inversion, and the energy on the transverse component is greatly reduced. Laterally variable splitting parameters, $\hat{\phi}_{\text{fast}}(x,y)$ and $\Delta\hat{t}_{\text{split}}(x,y)$, designed on the overburden reflection interval ($t \approx 2.5$–2.9 s) appear to account for most of the splitting-related signal over the reservoir interval ($t \approx 3.5$–4.0 s), and at the basement reflection ($t \approx 5.3$ s).

Model parameter estimates, $\hat{\phi}_{\text{fast}}(x,y)$ and $\Delta\hat{t}_{\text{split}}(x,y)$, from the overburden inversion of the 3D data set are shown in Figure 14. The locations of lines A, B, and C are indicated. Given that the data are inverted independently at each location, the parameter estimates are relatively robust and are summarized as, $\phi_{\text{fast}} \approx 90° \pm 20°$, and $\Delta t_{\text{split}} \approx 28 \pm 20$ ms. A large change in slope of both parameters occurs near crossline 1400. Interestingly, it is in this region that some of the largest data misfits occur, and where the input radial azimuth-sectored stack gathers deviate from the implicitly assumed form of symmetric traveltime variations as a function of azimuth as observed in the synthetic data of Figure 3.

Radial and transverse azimuth-sectored stack gathers before and after a reservoir-level splitting inversion are shown in Figure 15. A 300-ms time window below the strong reflection at approximately 3.6 s on crossline 1200 (see Figure 15a) is used for the objective function $E_T(\phi_{\text{fast}}, \Delta t_{\text{split}})$. Radial and transverse gathers input to the inversion are shown in Figure 15a and d. These are the output data from the overburden inversion (from

Figures 6b and 7b). Compensated radial and transverse gathers output from the reservoir-interval inversion are shown in Figure 15b and e, respectively. The difference between the input and output gathers is shown in Figure 15c (radial) and f (transverse).

Radial gathers after the overburden inversion (Figure 15a) show an anomalous behavior of azimuthal traveltime variations at the crest of the anticlinal structure ($t \approx 3.5$ s and 4.0 s near crossline 1350), downdip from the anticline, and along the basement reflection ($t \approx 5.3$ s near crossline 1300). These anomalous traveltime variations remain after the reservoir-interval inversion (Figure 15b). The transverse gathers are significantly weaker in amplitude (because the overburden inversion accounted for most of the transverse component energy), and there is not an easily visible difference between the input (Figure 15d) and output (Figure 15e) gathers. The difference displays of the radial (Figure 15c) and transverse (Figure 15f) gathers show the level of signal change produced by the reservoir-interval inversion.

It is not clear that the reservoir-interval inversion results in meaningful estimates of ϕ_{fast} and Δt_{split}. The input radial and transverse azimuth-sectored stack gathers clearly deviate from the patterns expected for C-wave splitting from HTI layers in a locally 1D earth, as seen in the synthetic examples. The objective function, $E_T(\phi_{\text{fast}}, \Delta t_{\text{split}})$, for each pair of radial and transverse gathers analyzed, will always yield a minimum, even if the input data are anomalous, and thus, the parameter estimates questionable.

Results shown in Figure 15 are representative of the reservoir-interval inversion applied to the full 3D data set.

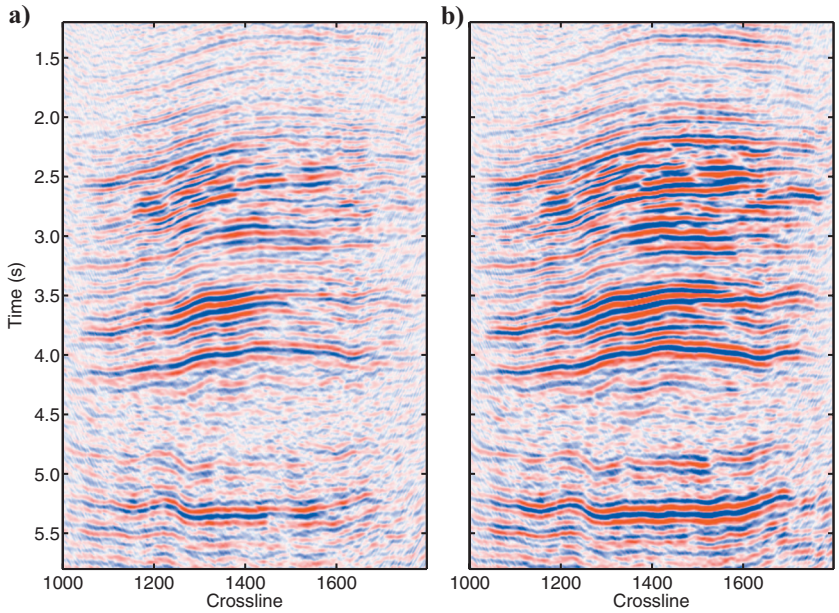

Figure 10. Radial component, full-azimuth stacks, line B. (a) Before overburden inversion and compensation. (b) After overburden inversion and compensation.

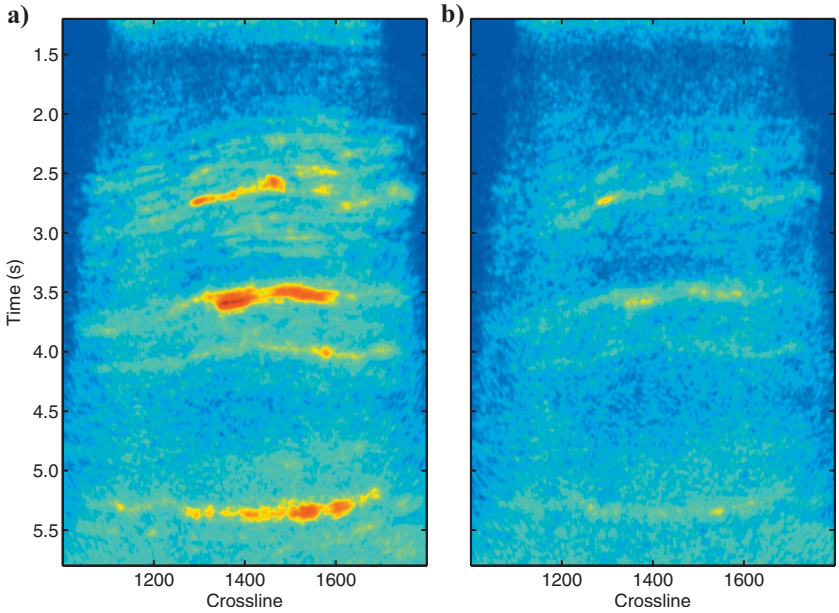

Figure 11. Transverse component, full-azimuth stacks, line B. (a) Before overburden inversion and compensation. (b) After overburden inversion and compensation.

DISCUSSION

A common approach to C-wave processing is to rotate the prestack data, R_x and R_y, to a presumed ϕ_{fast}. After rotation by a constant azimuth, the data are transformed to fast and slow data sets. These fast, slow data sets are then crosscorrelated over some time interval to estimate a laterally variable Δt_{split}. If stacked data are to be later analyzed, polarity reversal of subsets of the fast and slow prestack data is involved. The presumption as to which trace polarities must be reversed is dependent on the ϕ_{fast} used for rotation. Should this angle be in error, or vary laterally, degradation in stacked signal quality will result.

Generally, the initial rotation to fast-slow and crosscorrelation corrects for overburden splitting. Additional analysis for potentially deeper splitting strictly requires that the overburden splitting be layer stripped to accurately expose the deeper splitting. Note that the presumed azimuth used for rotation is often obtained from the regional stress direction, VSP analysis, P-wave azimuthal velocity analysis, or other means. It is not clear that a regional stress necessarily affects three-component surface seismic data to an observable degree. For data sparsely sampled in azimuth, an a priori rotation to fast-slow based on auxiliary data may be satisfactory. Such a constant-angle rotation will be problematic when ϕ_{fast} varies laterally. Given three-component data that are well sampled in azimuth, I feel that a more defensible approach is to estimate ϕ_{fast} directly from the data, where ϕ_{fast} is permitted to vary spatially.

The general philosophy behind the SEAC inversion is to obtain the simplest model that explains the data. A direct measure of the extent to which the data are explained is obtained through the postinversion transverse component (data

misfit). Laterally variable overburden estimates, ϕ_{fast} and Δt (Figure 14), explain the presumed splitting-related signal to the extent shown in the full-azimuth radial and transverse stacks (Figures 8–13). An approach that a priori rotates the prestack radial and transverse data to a presumed constant ϕ_{fast} would obviously be in error, and result in a larger data misfit.

SEAC layer stripping is somewhat analogous to velocity analysis. More reliable and meaningful results will be obtained when the inversion design windows are centered on high amplitude, laterally continuous, reflection events. Attempts at estimating splitting-parameter profiles that are finely sampled in time will likely prove problematic, in general. In addition, the splitting-induced Δt_{split} is actually incidence-angle (offset) dependent. Upon stacking over offset, the Δt_{split} estimate is a weighted average, dependent upon the offset (angle) distribution of the traces included in the stack that may impose an apparent spatial and temporal variability in the parameter estimates.

An important point to keep in mind, however, is that the data misfit indicates where the inverted data are not predicted by the model parameter estimates. As a result, it is not necessary for the inversion to account for the splitting anomalies in the model parameter estimates. The data misfit can potentially be interpreted as a potential fracture-anomaly volume. This fracture-anomaly volume is in itself an interpretable data set, and can indicate where additional inversions are needed to explain the data.

The overburden inversion parameter estimates are robust, and the improvement in the compensated full-azimuth radial stacks is obvious, as is the reduction in transverse-component energy. Additional reservoir-level and basement-level inversions produce less reliable parameter estimates, and marginal changes to the compensated radial and transverse component stacks. At this stage of analysis, a higher degree of confidence is assigned to the improvement in radial stack image quality than to the parameter estimates being directly interpretable in terms of subsurface fractures. The postoverburden inversion radial and transverse azimuth-sectored stack gathers deviate from the expected response of HTI layers in a locally 1D earth, as shown in Figure 15. This affects the reliability of the deeper inversions.

In general, the largest amount of energy remaining on the transverse component occurs near the crest of the anticlinal structure as observed in Figures 9 and 11. Errors in the PSTM velocity model will produce a discrepancy in the C-wave reflection points of opposite azimuth data (azimuths 180° apart), which becomes magnified for dipping structures, and causes the input data to deviate from the expected response. Another possible cause is that of local tilted transverse isotropy.

An obvious improvement to the algorithm would be to devise a reliability criterion based on how well the input radial and transverse azimuth-sectored stacks data agree with the expected response. The depth of the objective function minimum can also be used to assess the reliability of the model parameter estimates. Smoothing can be implicitly introduced into the inversion by processing several input gather pairs simultaneously (a block of 3×3 gather pairs to estimate the model parameters at the center of the block, for example).

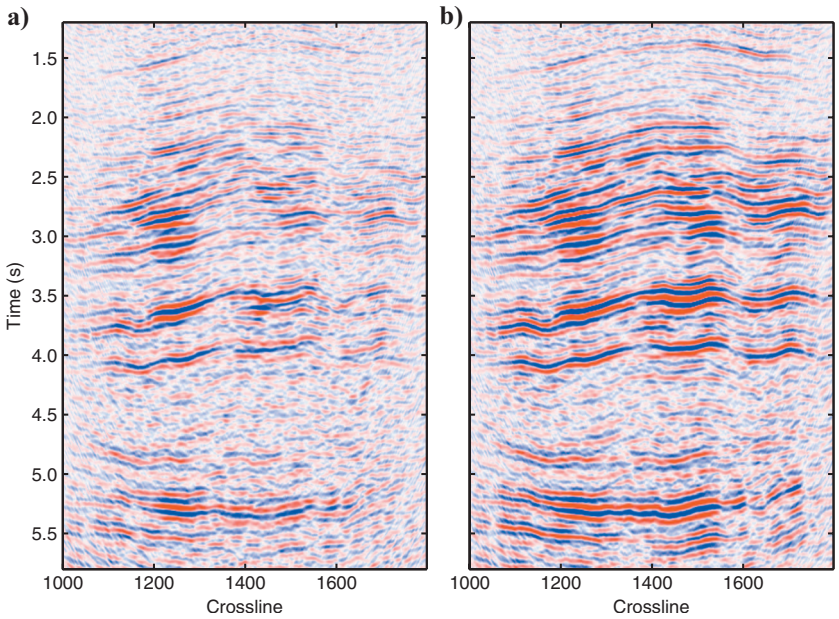

Figure 12. Radial component, full-azimuth stacks, line C. (a) Before overburden inversion and compensation. (b) After overburden inversion and compensation.

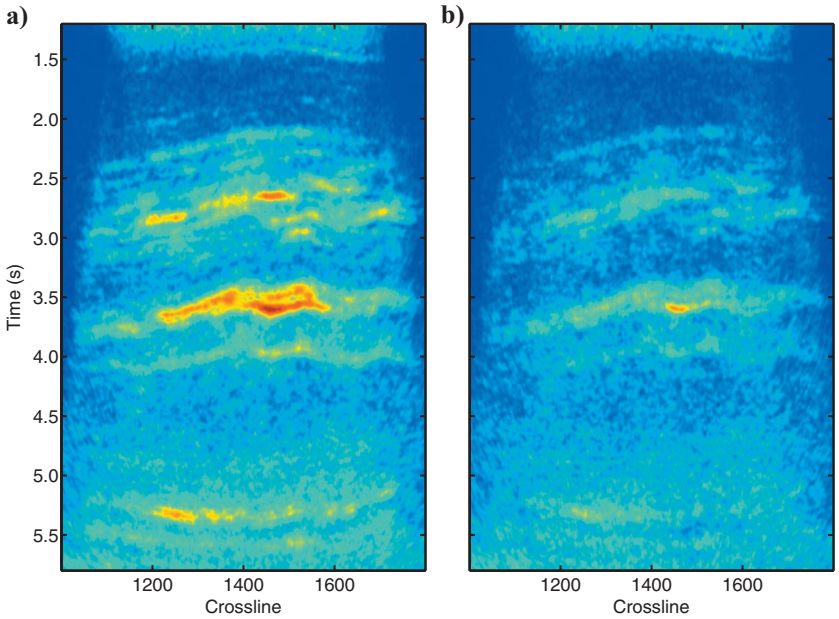

Figure 13. Transverse component, full-azimuth stacks, line C. (a) Before overburden inversion and compensation. (b) After overburden inversion and compensation.

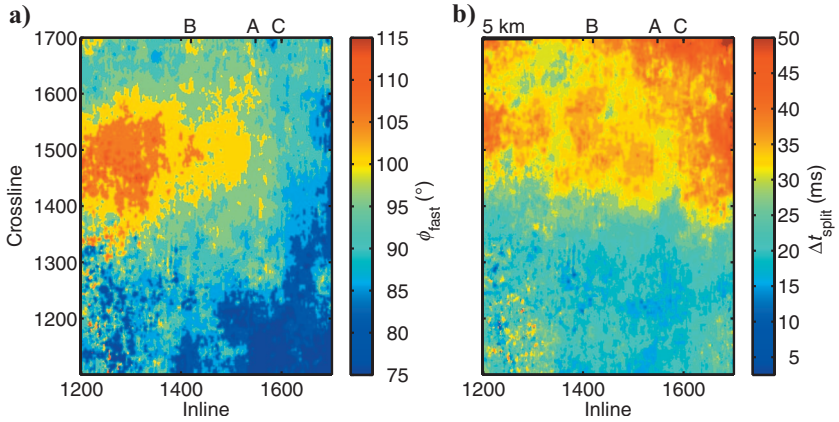

Figure 14. Splitting model-parameter estimates, overburden inversion. The locations of lines A, B, and C are noted. (a) Azimuth $\hat{\phi}_{fast}$. (b) Splitting magnitude $\Delta\hat{t}_{split}$.

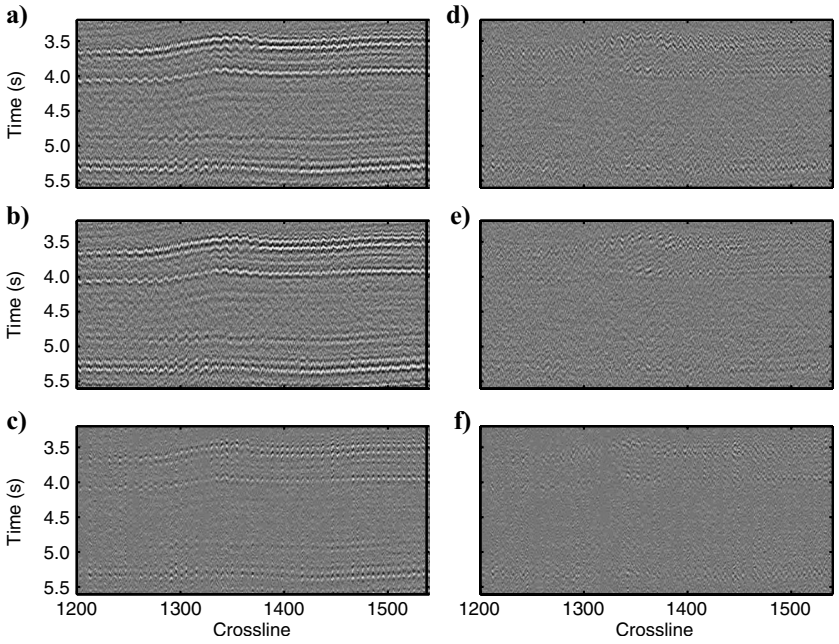

Figure 15. Data before and after a reservoir-level splitting inversion. (a) Input radial azimuth-sectored stack gathers. These data are the output from the overburden inversion. (b) Output radial gathers. (c) The difference between the input and output radial gathers. (d) Input transverse azimuth-sectored stack gathers. These data are the output from the overburden inversion. (e) Output transverse gathers. (f) The difference between the input and output transverse gathers.

CONCLUSIONS

C-wave SEAC makes use of the splitting signatures seen on radial and transverse component azimuth-sectored stacks. Parameter estimates, $\hat{\phi}_{fast}$ (the fast-azimuth principal direction) and $\Delta\hat{t}_{split}$ (the amount of shear-wave splitting), are obtained by a grid search over all prespecified parameter combinations. The algorithm rotates the input data to fast-slow data sets using a trial ϕ_{fast}, and applies a trial static shift to the slow data set of Δt_{split}, which is followed by an inverse rotation of the fast-slow data sets to radial-transverse data sets. The optimal parameter pair produces minimal energy on the output transverse component over a specified time window.

An implicit assumption is that of a locally 1D earth and shear-wave splitting produced by HTI layers. As a result, there are predictable patterns of azimuth-dependent traveltime variations on the radial component, and polarity reversals on the transverse component. The inverse problem will have difficulty predicting the data where these assumptions are violated.

A constant fast-azimuth direction is clearly not appropriate for this field data set. Although each input gather is inverted independently, the parameter estimates are robust in a spatial sense because the objective function has well-defined minima for the overburden inversion. Incorporation of lateral constraints into the inversion should be relatively straightforward, and become increasingly important when inverting for deeper splitting where the magnitude of Δt_{split} will be smaller than that of the overburden inversion.

The compensated radial data set is much more interpretable than is the input radial data set. The postinversion transverse data provides a quantitative, and interpretable, measure of the extent to which the estimated splitting parameters are able/unable to predict the input data.

ACKNOWLEDGMENTS

Peter Stewart of GX Technology masterfully processed the C-wave data through prestack time migration. Critical reviews by Richard Bale, Milo Backus, and Mauricio Sacchi greatly improved the signal-to-noise ratio of the original manuscript, as did discussion with Jim Gaiser. Thanks to Nick Bernitsas of GX Technology for permission to publish, and to Sinopec for permission to show the field data.

REFERENCES

Alford, R. M., 1986, Shear data in the presence of azimuthal anisotropy: 56th Annual International Meeting, SEG, Expanded Abstracts, 476–479.

Bale, R. A., J. Li, B. Mattocks, and S. Ronen, 2005, Robust estimation of fracture directions from 3-D converted-waves: 75th Annual International Meeting, SEG, Expanded Abstracts, 889–892.

Bowman, J. R., and M. Ando, 1987, Shear-wave splitting in the upper-mantle wedge above the Tonga subduction zone: Geophysical Journal of the Royal Astronomical Society, **88**, 25–41.

Chevrot, S., 2000, Multichannel analysis of shear wave splitting: Journal of Geophysical Research, **105**, 579–590.

Fryer, G. J., and L. N. Frazier, 1984, Seismic waves in stratified anisotropic media: Geophysical Journal of the Royal Astronomical Society, **78**, 691–710.

———, 1987, Seismic waves in stratified anisotropic media – II. Elastodynamic eigen-solutions for some anisotropic systems: Geophysical Journal of the Royal Astronomical Society, **91**, 73–101.

Fukao, Y., 1984, Evidence from core-reflected shear waves for anisotropy in the earth's mantle: Nature, **309**, 695–698.

Gaiser, J. E., 1999, Applications for vector coordinate systems of 3-D converted-wave data: The Leading Edge, **18**, 1290–1300.

Gumble, J. E., and J. E. Gaiser, 2006, Characterization of layered anisotropic media from prestack PS-wave-reflection data: Geophysics, **71**, no. 5, D171-D182.

Keith, C. M., and S. Crampin, 1977, Seismic body waves in anisotropic me-

dia: Synthetic seismograms: Geophysical Journal of the Royal Astronomical Society, **94**, 225–243.
Kennett, B. L. N., 1983, Seismic wave propagation in stratified elastic media: Cambridge University Press.
Lefeuvre, F., L. Nicoletis, V. Ansel, and C. Cliet, 1992, Detection and measure of the shear-wave birefringence from vertical seismic data: Theory and applications: Geophysics, **57**, 1463–1481.
Lev, E., M. D. Long, and R. D. van der Hilst, 2006, Seismic anisotropy in eastern Tibet from shear-wave splitting reveals changes in lithospheric deformation: Earth and Planetary Science Letters, **251**, 293–304.
Levin, V., W. Menke, and J. Park, 1999, Shear wave splitting in the Appalachians and the Urals: A case for multilayered anisotropy: Journal of Geophysical Research, **104**, 975–993.
Li, X. Y., 1998, Fracture detection using P-P and P-S waves in multicomponent seafloor data: 68th Annual International Meeting, SEG, Expanded Abstracts, 2056–2059.
Long, M. D., 2006, Anisotropy and deformation in the earth's mantle: Seismological observations, geodynamical models, and laboratory experiments: Ph.D. thesis, Massachusetts Institute of Technology.
Silver, P. G., and W. W. Chan, 1991, Shear wave splitting and subcontinental mantle deformation: Journal of Geophysical Research, **96**, 429–454.
Thomsen, L., 1988, Reflection seismology over azimuthally anisotropic media: Geophysics, **53**, 304–313.
Thomsen, L., I. Tsvankin, and M. C. Mueller, 1995a, Adaptation of split shear — wave techniques to coalbed methane exploration: 65th Annual International Meeting, SEG, Expanded Abstracts, 301–304.
———, 1995b, Layer-stripping of azimuthal anisotropy from reflection shear-wave data: 65th Annual International Meeting, SEG, Expanded Abstracts, 289–292.
———, 1999, Coarse-layer stripping of vertically variable azimuthal anisotropy from shear-wave data: Geophysics, **64**, 1126–1138.
Vidale, J. E., 1986, Complex polarization analysis of particle motion: Bulletin of the Seismological Society of America, **71**, 1511–1530.
Winterstein, D. F., and M. A. Meadows, 1991a, Changes in shear-wave polarization azimuth with depth in Cymric and Railroad Gap oil fields: Geophysics, **56**, 1349–1364.
———, 1991b, Shear-wave polarizations and subsurface stress directions at Lost Hills field: Geophysics, **56**, 1331–1348.